# Benefits of Smoothing Backgrounds and Radar Reflectivity Observations for Multiscale Data Assimilation with an Ensemble Kalman Filter at Convective Scales: A Proof-of-Concept Study

JAGDEEP SINGH SODHI<sup>a</sup> AND FRÉDÉRIC FABRY<sup>a,b</sup>

<sup>a</sup> Department of Atmospheric and Oceanic Sciences, McGill University, Montreal, Quebec, Canada
<sup>b</sup> Bieler School of Environment, McGill University, Montreal, Quebec, Canada

(Manuscript received 28 May 2021, in final form 17 December 2021)

ABSTRACT: In the ensemble Kalman filter (EnKF), the covariance localization radius is usually small when assimilating radar observations because of high density of the radar observations. This makes the region away from precipitation difficult to correct using only radar data stating "no echo" if no other observations are available, as there is no reason to correct the background. To correct errors away from innovating radar observations, a multiscale localization (MLoc) method adapted to dense observations like those from radar is proposed. In this method, different scales are corrected successively by using the same reflectivity observations, but with a different degree of smoothing and localization radius at each step. In the context of observing system simulation experiments, single and multiple assimilation experiments are conducted with the MLoc method. Results show that the MLoc assimilation updates areas that are away from the innovative observations and improves on average the analysis and forecast quality in single cycle and cycling assimilation experiments. The forecast gains are maintained until the end of the forecast period, illustrating the benefits of correcting different scales.

KEYWORDS: Convective storms; Kalman filters; Short-range prediction; Data assimilation; Ensembles; Radars/radar observations

### 1. Introduction

One of the uses of data assimilation (DA) systems is to generate initial conditions for numerical weather prediction (NWP) models by optimally combining a short-range forecast and observations. For convective-scale forecasting, ensemblebased DA methods (Houtekamer and Zhang 2016) such as the ensemble Kalman filter (EnKF) have been widely used in research and operational centers for their ability to easily estimate and use flow-dependent covariances. Numerous studies have documented the benefits of applying the EnKF for convective-scale forecasting (e.g., Schwartz et al. 2015). However, the higher computational cost associated with running highresolution NWP models limits the number of ensemble members that can be used. Since ensemble-based DA methods compute the error covariances from the members, the limited ensemble size affects the accuracy of error relationships in the covariance matrix due to sampling errors (Necker et al. 2020). As error covariances generally diminish with distance, so does the accuracy with which they can be computed given a limited ensemble size. To avoid problems associated with noisy correlations at large distances, covariance localization (Hamill et al. 2001; Houtekamer and Mitchell 2001) is implemented in the EnKF systems. The localization radius determines the distance beyond which the error covariances are deemed untrustworthy and are set to zero; hence, any state variable outside this radius is not updated by the observational information. The magnitude of the covariance localization depends upon the ensemble size (Lorenc 2003), the density of the

Corresponding author: Jagdeep Singh Sodhi, jagdeep.singh.sodhi@mail.mcgill.ca

observations (Periáñez et al. 2014), the effective resolution of the NWP model (Miyoshi and Aranami 2006; Buehner and Shlyaeva 2015) and the type of the observation and the state variable (Anderson 2007).

Traditional assimilation approaches have been designed to make the best use of point observations that were often spaced by hundreds of kilometers. These sparse point observations are often assimilated with a localization radius of O(1000) km for synoptic modeling. In contrast, weather radars provide dense observations both spatially and temporally, requiring much smaller localization radii. Operational radars measure the spatial distribution of hydrometeors in precipitation-producing storms in great detail. Radar observations, when assimilated using the EnKF, have been shown to improve the quality of short-range forecasts (Aksoy et al. 2009, 2010; Dowell et al. 2011). One shortcoming of radar observations is that they do not provide much direct information on dynamically and thermodynamically important fields that influence the future evolution of storms, thus making properly assimilating radar data a challenging task (Fabry and Meunier 2020). Furthermore, the horizontal localization radius used in the EnKF for radar DA is usually in the range of 5-20 km (Sobash and Stensrud 2013, and references therein) given model resolutions of 1-3 km. This is because, with high data density and limited ensemble size, the localization radius must be reduced to prevent over constraining the analysis (this is known as the rank problem; Lorenc 2003). Indeed Ying et al. (2018) and references therein showed that smaller localization radii perform best for a relatively small ensemble size. Since radar provides its best information in rainy areas, a shorter localization leaves regions away from echo areas uncorrected. And given the clustered nature of

radar echoes, the innovative information being only available where precipitation occurs, a shorter localization radius restricts the propagation of radar information from echodense locations to echo-sparse locations. Since convective-scale models resolve small- to large-scale flows, it is critical to constrain errors that are present at all these scales.

To reduce errors across multiple scales using ensemble-based DA methods, multiscale localization methods are being actively researched and adopted by the DA community (e.g., Caron and Buehner 2018; Caron et al. 2019). Zhang et al. (2009) proposed the successive covariance localization method, where the observation density and localization radius depends on the scale to be corrected. The errors at synoptic scales were corrected by assimilating a small subset of radar super-observations (also known as super-obbing; Weng and Zhang 2012) with a large localization radius. In scale-dependent localization (Buehner 2012; Buehner and Shlyaeva 2015), different localization radii are applied to different range of spatial scales in the background error covariances, and all the observations are assimilated in one go. Miyoshi and Kondo (2013) proposed a dual-localization (DL) method, in which independent analyses are produced by applying appropriate localization radii and then combined to generate the final analysis. To obtain the synoptic-scale correction in the DL method, the background ensemble perturbations were spatially smoothed and synoptic observations were assimilated with a wider localization radii. Yang et al. (2017) demonstrated the benefits of the DL method by applying it to improve the prediction of an actual heavy rainfall event. The multiscale alignment method of Ying (2019) showed value in reducing displacement errors across scales. Wang et al. (2021) proposed the so-called multiscale local gain form ensemble transform Kalman filter. The study noted that the multiscale method gained predictability by 12 h to 1 day. None of these methods have explicitly smoothed both the observations and background ensembles to correct larger scales patterns, however. Yet we believe such an approach has merit, because patterns of large-scale covariance between observations and state variables are more likely to be revealed by using averaged observations than by using point observations as well as by computing covariances using smoothed backgrounds. Note that this is somewhat similar to the multiscale approach of Ying (2020) who used spectrally filtered observations and backgrounds. We also believe that for the highly structured precipitation fields at convective-scale, spatial smoothing should perform better than spectral filtering for high-resolution grids because it does not assume periodicity: convective precipitation is generally organized in spatial structures such as cells and clusters; their evolution will therefore be driven by local fields and not by periodic structures such as waves. Radar data are very amenable to such an approach, as averaged reflectivity can be used to correct large-scale features, while for smaller scales, high-resolution reflectivity can be assimilated.

We believe both the backgrounds and observations should be smoothed for the proper extraction of the distant correlations needed to correct fields far away from innovative observations. Our goal in this work is to evaluate the performance of such an approach relative to the traditional single-scale assimilation for a few convective events.

### 2. Method

To overcome the limitations of using a small and single localization radius when assimilating radar reflectivity observations for convective-scale forecasting, a new assimilation approach referred to as MLoc (described in section 2b) is presented and evaluated: first, the larger scales are corrected by aggressively smoothing both the background state and reflectivity observations and allowing the correction to be spread over the whole domain by not applying any localization given that the domain size is not much larger than the smoothing radius; then, similarly, a smaller smoothing radius for intermediate scales is applied with a medium value of localization; and finally, the high-resolution backgrounds and observations at all scales are used with a small localization radius. The performance of this method is compared with a traditional single localization (SLoc) experiment in the context of observing system simulation experiments (OSSE) in a perfect-model setup. We chose to use an OSSE-based approach because we lack observations to evaluate the performance of both methods for fields other than precipitation.

# a. NWP model and DA system

The NWP model chosen for this study is the Weather Research and Forecasting (WRF) v4.0.2 (Skamarock et al. 2019) Model with the Advanced Research WRF (ARW) dynamical core. The model horizontal grid is 150 km  $\times$  150 km with a horizontal grid spacing of 1 km and 51 model levels in the vertical direction. The model microphysics follows the Thomson scheme (Thompson et al. 2008), the longwave and shortwave radiation schemes are the Rapid Radiative Transfer Model for Global Climate Models (RRTMG; Iacono et al. 2008), the land surface model scheme is the Unified Noah land surface model (Tewari et al. 2004), and the Mellor-Yamada–Janjić (MYJ) planetary scheme (Janjić 1994) is used in the boundary layer. The cumulus parameterization is switched off. The dry potential temperature  $\theta$  is used in the dynamics (use\_theta\_m = 0); therefore, the WRF variables perturbation dry potential temperature "T" and perturbation moist potential temperature THM are the same, and both are the perturbation dry potential temperature.

For the experiments, the High-Resolution Rapid Refresh (HRRR) model analysis is used to generate 51 ensemble members using the three-dimensional variational approach with the CV3 option of the WRF Data Assimilation (WRFDA) system. Among the generated 51 members, a member is randomly chosen to be the Truth (nature) and the remaining 50 members are used for the OSSE experiments. To spin up the dynamics, 1-h forecasts are produced for all 50 members before starting the assimilation experiments (Fig. 1). These 50 members will be used as background for all of the DA experiments.

The proper handling of boundary conditions (BC) required a few manipulations to ensure that the Truth and the members did not have similar BC by design. A WRF boundary file is generated from the HRRR analysis with updates every 1 h for a 4-h forecast for the nature run. Then the BC for the Truth is set to the BC from HRRR plus a time-independent

FIG. 1. Flowchart depicting the process of creating the initial conditions for the Truth and background runs.

deviation corresponding to the difference between the Truth member (randomly selected) and the HRRR analysis at initial time. For specifying the BC of members, we faced a technical difficulty that required us to modify default BC tendencies. A single template WRF boundary file is generated from the HRRR analysis that is then used to create 50 WRF boundary files, one per member. These boundary files are later updated with the information from the corresponding member using the Data Assimilation Research Testbed (DART) program update\_wrf\_bc. But when the BC are updated by update\_ wrf\_bc for all members, the tendencies are recomputed by default such that the BC at the end time become identical for all members. To prevent this BC spread collapse at the end time, we updated the tendencies such that the BC at end time become the BC of the HRRR at the end time plus the deviation between the member and the ensemble mean at the initial time. In other words, the BC at the end time become such that the mean for all BC is the HRRR analysis at the end time and the ensemble spread of the BC is identical to the spread at the initial time.

For the DA, the ensemble adjustment Kalman filter (EAKF; Anderson 2001) within the DART (Anderson et al. 2009) is used. The Gaspari and Cohn (1999) function is used for covariance localization. Synthetic radar reflectivity observations from nine model eta levels (0.949, 0.818, 0.706, 0.519, 0.404, 0.297, 0.241, 0.1976, 0.1553) are directly harvested from the Truth. We assume that we have radar observations available everywhere in the domain. The state variables of WRF updated by the EAKF are the perturbation geopotential PH; the perturbation dry air mass in column MU; the surface pressure PSFC; the three components of wind "U," "V," and "W"; the perturbation potential temperature T/THM; and the mixing ratios of water vapor QVAPOR, rainwater QRAIN, cloud water QCLOUD, graupel QGRAUP, snow QSNOW, and ice QICE. The radar forward operator in DART is not used to compute the reflectivity values; therefore, the reflectivity variable (REFL\_10CM) is included among the state variables during assimilation, and DART will have direct access to the REFL\_10CM fields in the background members during the assimilation process. For all experiments conducted in this paper, the REFL\_10CM field in the Truth and in the background members are calculated using Reisner et al. (1998). The values of reflectivity below 5 dBZ are set to 5 dBZ. It is assumed that the observation errors are uncorrelated, and the errors are added to the observations by randomly drawing a

value from a Gaussian distribution with 0 mean and a specified error variance of  $9 \text{ dB}(Z^2)$  [3-dB(Z) standard deviation].

# b. Multiscale localization (MLoc) method

A three-step MLoc method is designed with the imperfect assumption that there is no cross correlation between errors at different scales. These three steps are performed one after the other (iteratively) where the analysis from the previous step becomes the background of the next step while using the same set of observations. In the first two steps, a two-dimensional Gaussian filter (GF) is used with different width r to smooth (in the x and y directions) the REFL\_10CM and the other WRF state variables excluding the hydrometeor fields (QRAIN, QCLOUD, QGRAUP, QSNOW, QICE) in the background members. Synthetic observations are obtained by taking REFL\_10CM with added measurement errors  $[\sigma^2 = 9 \text{ dB}(Z^2)]$ and smoothing them with the same GF. The hydrometeor variables are excluded from the state variables during assimilation in steps 1 and 2; that is, they will not be updated by the filter. The reason for doing so will be explained in section 3a. Spatial smoothing ensures the suppression of small-scale (high frequency) variability, revealing the existence of weak covariances at large and intermediate scales. The third step is to correct errors of all fields (state variables) at all scales by using the background and observations at their original resolutions.

Since the same observations with the same observation error are used three times (number of assimilation steps; n=3) to compute three innovations, their weight must be reduced by a factor of 3 at each step for assimilation to remain optimal (this is a similar approach to what was done by Emerick and Reynolds (2013) in the context of an ensemble smoother with multiple data assimilations). As a result, instead of 9 dB( $Z^2$ ), the stated observation error in the final high-resolution step will be given by

$$\sigma_{\text{obs}}^2 = 9n \quad [dB(Z^2)]. \tag{1}$$

At larger scales, the fields are smoothed with a GF with a width r, and those smoothed data will have a stated observation error given by

$$\sigma_{\text{obs}}^2 = \frac{9}{\pi r^2} n \quad [dB(Z^2)], \tag{2}$$

with  $\pi r^2$  representing the equivalent number of pixels being smoothed at 1-km resolution by the GF if r is in kilometers.

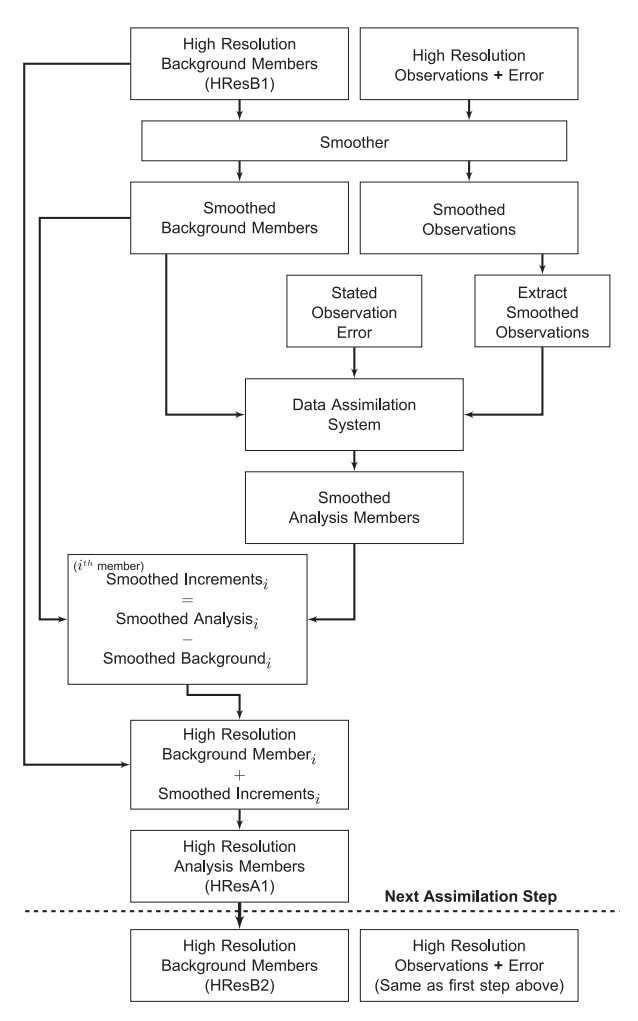


FIG. 2. Flowchart of the large-scale correction step. The middle-scale correction step is algorithmically similar to this one except for the less aggressive filter of the smoother.

The MLoc assimilation hence proceeds as follows (see also the flowchart of step 1 in Fig. 2): The 50 high-resolution backgrounds at step 1 (HResB1) and the observations with their errors are first smoothed using the GF; that is, each background member field that is included in the state variables (PH, MU, PSFC, U, V, W, T/THM, and QVAPOR) and the resulting simulated observations (REFL\_10CM) are smoothed and so is REFL\_10CM in the Truth. The radius of smoothing in this step is large enough (r = 50 km) relative to the domain size (150 km  $\times$  150 km) that only one observation per observation level from the middle of the domain is assimilated, and the error for each observation is given by Eq. (2). Given the small domain size, localization is not applied for this step, allowing the observational information to influence all the grid points. These smoothed fields and observations are then used by the DA system to compute smoothed increments to background fields. After assimilation, the smoothed analysis and the smoothed background are used to extract increments and estimate a new analysis using

$$X_{HA} = X_{HB} + (X_{SA} - X_{SB}),$$
 (3)

for dynamical and thermodynamic fields. In Eq. (3), X is a generic symbol for all of the dynamical and thermodynamic state variables (PH, MU, PSFC, U, V, W, T/THM, and QVA-POR) modified by the assimilation, and the subscripts HA, HB, SA, and SB are for high-resolution analysis, high-resolution background, smoothed analysis, and smoothed background, respectively. The resulting fields from Eq. (3) are hence the analysis after step 1 (HResA1) for which the largescale patterns are corrected. The HResA1 generated in the first step will become the background (HResB2) in step 2. In the second step, the HResB2 and the observations with their errors are then smoothed with r = 5 km. The cutoff radius is 30 km in the horizontal plane and 3 km in the vertical direction. The synthetic reflectivity is extracted every 15 km (horizontal) with the observation error calculated using Eq. (2). The rest of the procedure of producing the analysis (HResA2) by the end of the second step is similar to that of step 1. At the end of the second step, the updated state variables are PH, MU, PSFC, U, V, W, T/THM, and QVAPOR. The third step is a normal DA procedure (without smoothing) where the analysis (HResA2) of the previous step becomes the background of the current step (HResB3). In this step, hydrometeor fields are also included in the state variables. The cutoff radius in the horizontal plane and vertical direction is 3 km. The synthetic reflectivity observations are extracted every 1 km (horizontal) from the Truth, and the error associated with the observations is calculated from Eq. (1). The final analysis (HResA3) is used to produce forecasts for the MLoc experiments.

The choices for the localization scales, data density, and number of scales of assimilation are dictated by several constraints. First at any scale, the radius of influence (ROI;  $2 \times$ cutoff radius) must be such that the number of independent constraints influencing any grid point does not vastly exceed the number of members so as not to collapse the ensemble spread (Lorenc 2003). Therefore, for an ensemble of 50 members, the ROI is limited to about 3 times the data spacing (6 times the data spacing for the cutoff radius; Gaspari and Cohn 1999). Second, since we want the corrections done with one smoothing radius to be as independent as possible from those done with the next smoothing radius, the next scale should be on the order of 10 times the smoothing radius from the previous one (because the cutoff diameter is 12 times the data density). Given our domain size, this imposes a threescale approach, roughly an order of magnitude apart. In the vertical direction, at smaller scales, the cutoff radius of 3 km was chosen from work by Dowell et al. (2011) and Dawson et al. (2012). It is also appropriate to use the same localization distance in the vertical than in the horizontal on the grounds that, at such scales, error correlation patterns become more isotropic in three dimensions. But once the horizontal smoothing exceeds 50 km, such a vertical cutoff radius does not make sense, and it was removed for the largest scales to allow the smoothed observations to innovate the whole atmosphere (all vertical levels). Our choice was guided by these principles, although no specific effort was done to fine-tune the values, because work by Ying et al. (2018) shows that

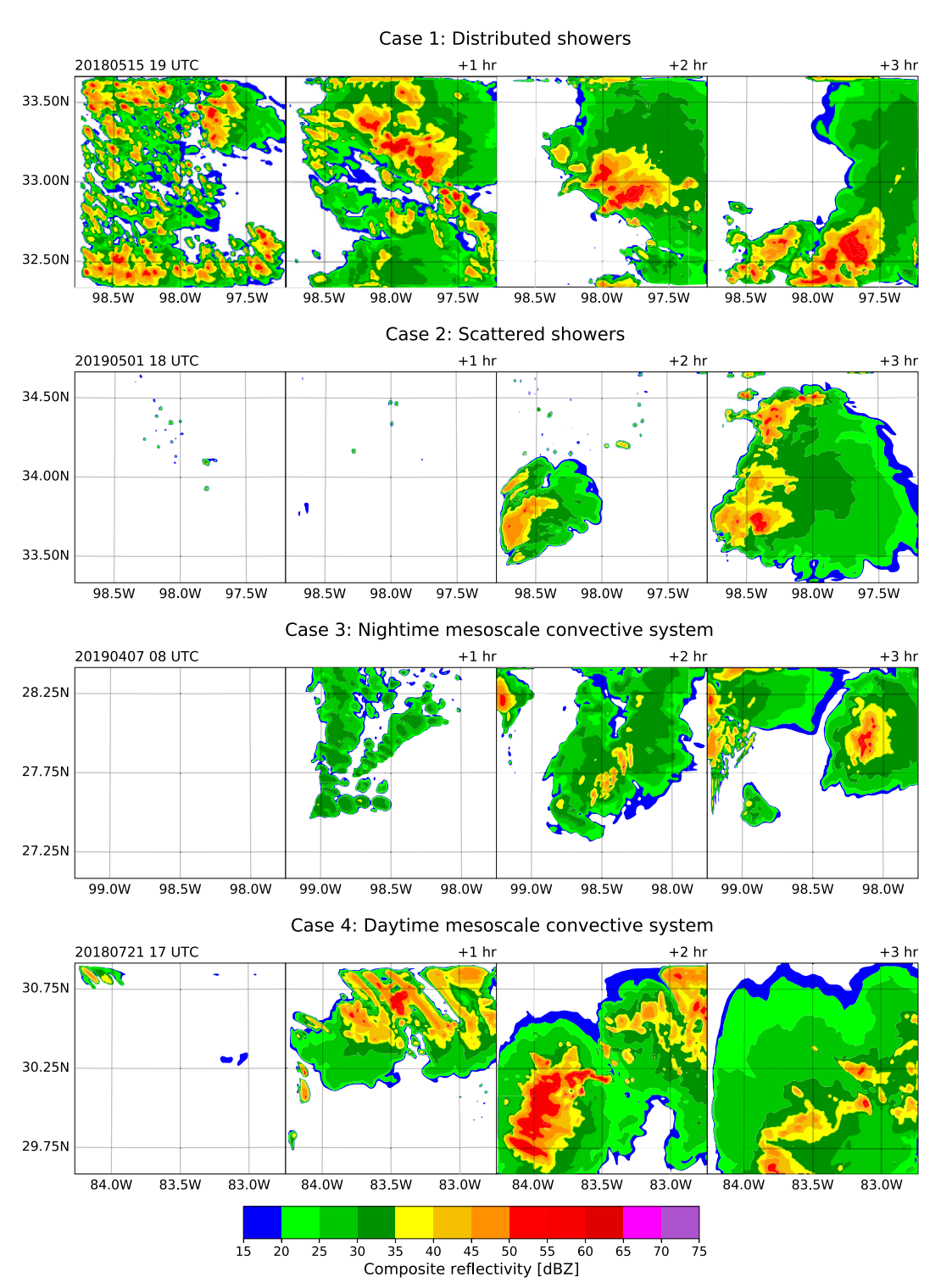


FIG. 3. Time evolutions of composite reflectivity plots for all of the cases (Truth) considered in this study, where composite reflectivity is the peak reflectivity in the column. The four cases are (top) distributed showers, (top middle) scattered showers, (bottom middle) nighttime mesoscale convective storms, and (bottom) daytime mesoscale convective storms. The start of assimilation time is shown as "YYYYMMDD HH" UTC, where Y, M, D, and H denote year, month, day, and hour, respectively. Note the coverage of precipitation echoes at the initial time and 2 h after because these influence the relative performance of multiscale assimilation as compared with the single-scale one.

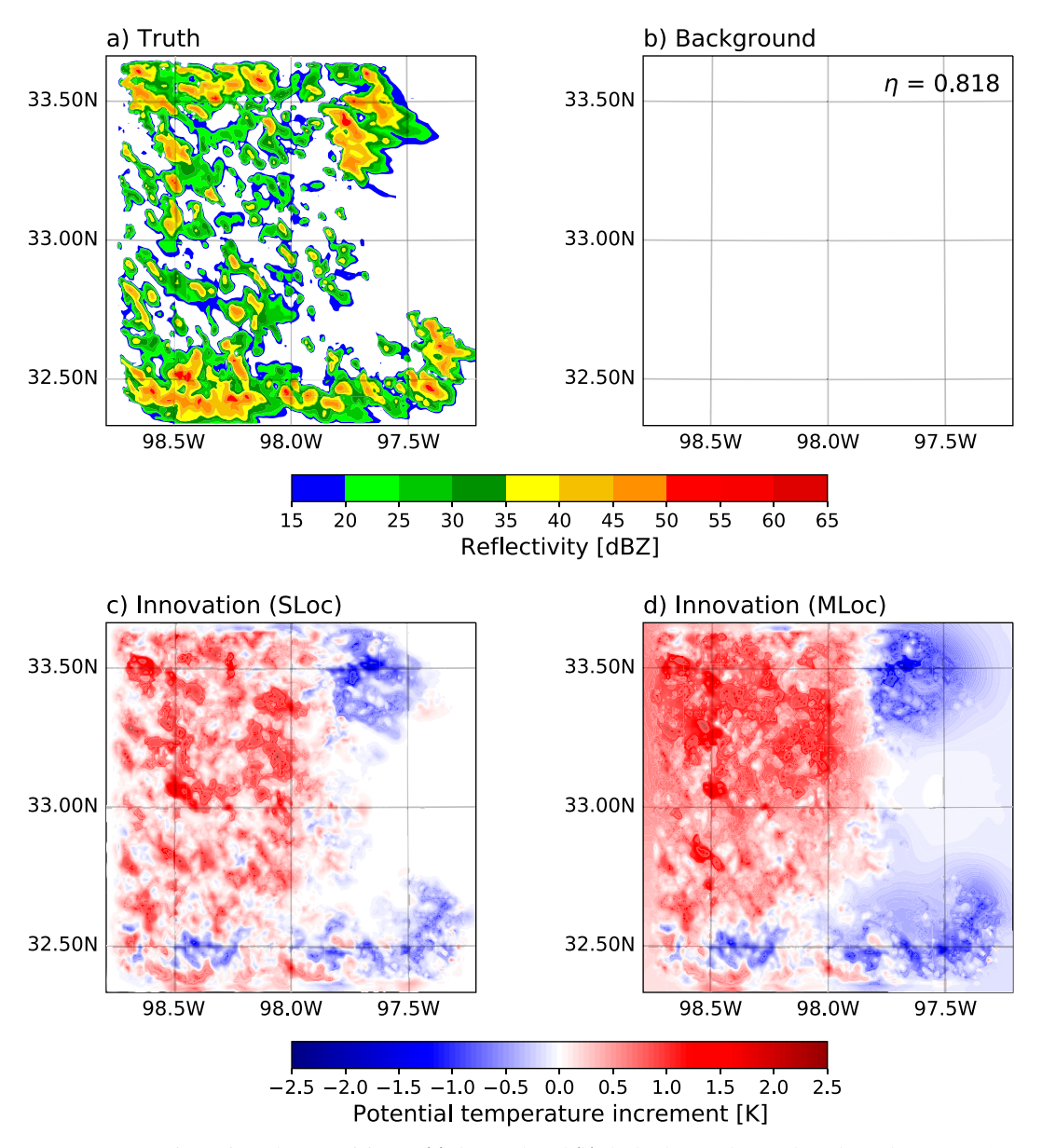


FIG. 4. Comparison, given the reflectivity for (a) the Truth and (b) the background of a selected member of case 1 at eta level 0.818, between the change in potential temperature resulting from DA using (c) SLoc and (d) MLoc at that same eta level.

selecting ROI  $\pm 50\%$  away from optimum still yields good results. We did not perceive that the exact tuning of those parameters would change the results significantly, and we saw this work as a proof of concept rather than as an optimization exercise that will require many more cases. If data were only available in a subset of the domain, smoothing of observations and of simulated observations and state variables could be limited to those regions, and the rest of the process would continue as described above.

# c. Experimental design

To evaluate the performance of the MLoc method, an SLoc assimilation experiment is undertaken to act as a reference. It

is similar to the third step of the MLoc method; that is, the cutoff radius is 3 km in both the horizontal and vertical directions, and observations are extracted every 1 km from the Truth. In SLoc, the observation error variance is set to 9 dB( $\mathbb{Z}^2$ ). For the selection of localization radius, experiments with cutoff radius of 3, 6, and 9 km with a fixed vertical cutoff radius of 3 km were conducted. It was found in the experiments that after multiple assimilation cycles, the 3-km cutoff radius performed better (results not shown) than other experiments. Factors such as the number of observations near each grid point (rank problem/degree of freedom; Lorenc 2003) and model resolution were also

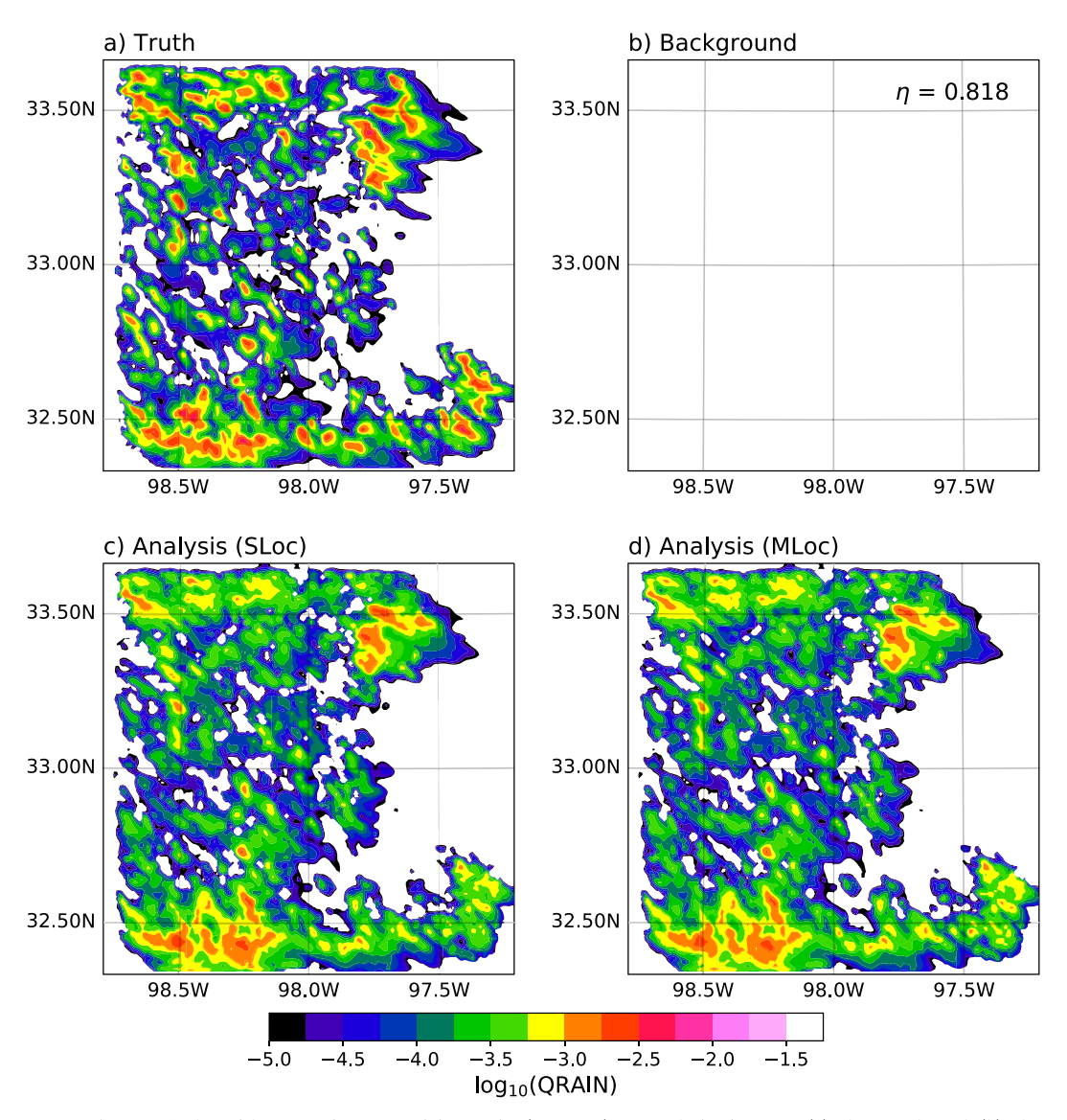


FIG. 5. Base-10 logarithm of rainwater mixing ratio (QRAIN) at analysis time for (a) the Truth and (b) the background, as well as after the first assimilation using (c) SLoc and (d) MLoc for the same member and eta level as in Fig. 4.

considered while making the choice for the cutoff radius in the single localization experiments as well as the choice of cutoff radius and data density for the multiscale experiments.

The four cases chosen for the experiments are shown in Fig. 3. These cases have varied convective structures to test the performance of the MLoc method in different conditions. Two separate experiments are performed. First, to understand how the MLoc performs initially, a single cycle experiment for both MLoc and SLoc is conducted after which a forecast of 1 h is generated and results are compared for both the analysis and the forecast. Then, a cycling experiment is conducted to evaluate the performance of the approach in the context of cycled assimilation.

### 3. Results

## a. Single cycle assimilation experiment

For case 1 (distributed showers), Fig. 4 shows the reflectivity field of the Truth, the background, and the potential temperature  $\theta$  increments (analysis minus background) at eta level 0.818 for a selected member after the assimilation of radar reflectivity observations at one time. Since the reflectivity field of the background (Fig. 4b) is different from that of the Truth, both assimilation approaches are able to add increments relative to the background where radar echoes are observed (Fig. 4a). However, the increments in SLoc are confined to the areas where reflectivity values are different between the background and the observations due to the use

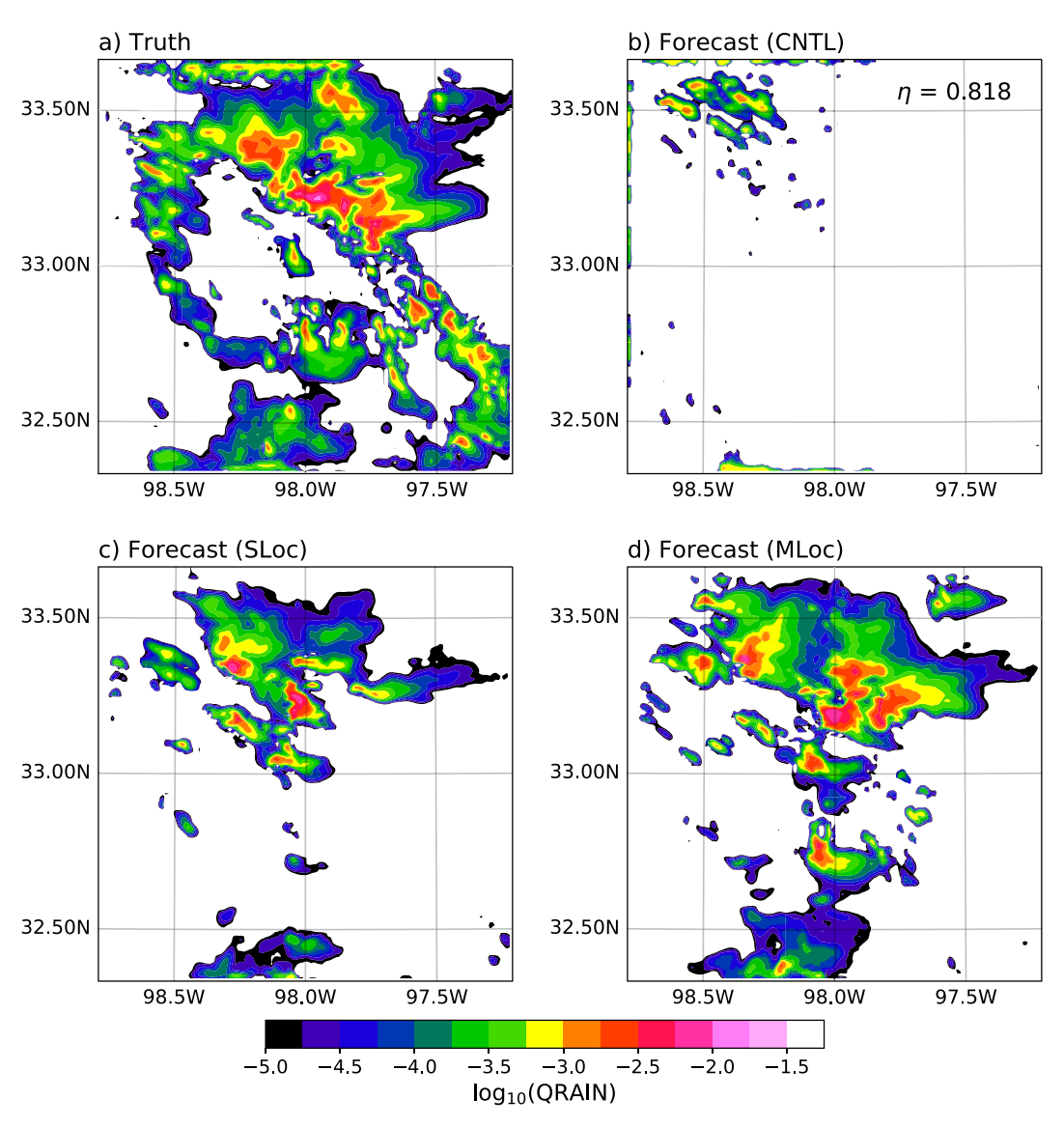


FIG. 6. Base-10 logarithm of QRAIN after a 1-h forecast for (a) the Truth, (b) the CNTL (forecast without assimilation of any observations), (c) SLoc, and (d) MLoc for the same member and eta level as in Fig. 4.

of a smaller localization radius. In comparison, for the MLoc approach designed to correct fields at different scales, the increments resulting from observations are spread farther from the precipitation observations and are also smoother. For the same case and member and at the same eta level, the base-10 logarithm of rainwater mixing ratio after assimilation is shown in Fig. 5. Because of the good correlation between reflectivity and QRAIN, the DA system placed QRAIN in the domain almost identically in both assimilation approaches. The most notable differences are slightly smoother fields and a small extension of very weak rainfall in the MLoc experiment relative to the SLoc one, but even these are difficult to visually detect in Fig. 5. To assess the performance of both experiments after the first assimilation, the model is run multiple times for an hour using successively

as initial conditions the original backgrounds without assimilation, and the SLoc and MLoc analyses. These are then compared with the Truth run. Figure 6 illustrates the resulting QRAIN field of the member shown in Figs. 4 and 5. For the SLoc assimilation approach (Fig. 6c), the QRAIN field that had almost similar structure as the Truth at analysis time (Fig. 5c v. Fig. 5a) largely reverted to the preassimilation trajectory of the background (Fig. 6b). It can be inferred that the fields that drive the precipitation process were not adjusted correctly to sustain the convection placed in the model domain during assimilation. In contrast, the forecast from the MLoc approach, though still far from the Truth run, is visually closer to it with more of the added convection surviving after an hour. The key difference between SLoc and MLoc is that the fields in MLoc have also received

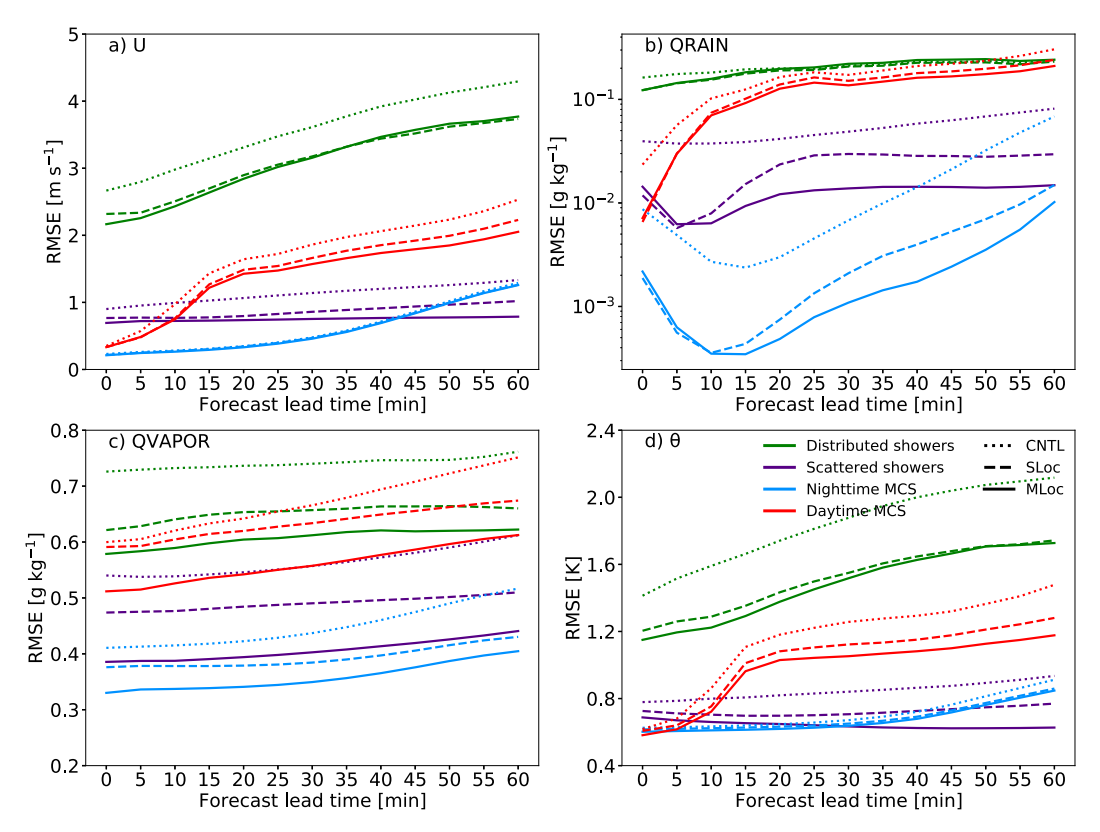


FIG. 7. Comparison of ensemble-averaged RMSE of CNTL (forecast without assimilation of any observations), SLoc, and MLoc for (a) U-component wind (WRF variable U), (b) QRAIN, (c) water vapor mixing ratio (QVA-POR), and (d) potential temperature ( $\theta$ ) fields for all cases.

large- to medium-scale increments, whereas in SLoc only small-scale patterns were updated.

A more quantitative evaluation was then performed. The ensemble-averaged root-mean-square error (RMSE) for all variables *x* for both SLoc and MLoc were computed using

RMSE = 
$$\frac{1}{M} \sum_{m=1}^{M} \left[ \sqrt{\frac{1}{N} \sum_{n=1}^{N} \left( x_{mn}^{f} - x_{n}^{t} \right)^{2}} \right],$$
 (4)

where M is the total number of ensemble members, N is the total number of grid points in a member, and the superscripts t and f stand for Truth and forecast respectively. The RMSE is calculated for the WRF U-component wind U, rainwater mixing ratio (QRAIN), water vapor mixing ratio (QVAPOR), and potential temperature  $\theta$  fields for all cases. Then, the RMSE ratio, which is the ratio of ensembled-averaged RMSE of MLoc and SLoc, is given by

$$RMSE_{ratio} = \frac{RMSE_{MLoc}}{RMSE_{SLoc}}.$$
 (5)

Figure 7 shows the RMSE for all the cases from analysis time up to 1-h forecast for U, QRAIN, QVAPOR, and  $\theta$  fields. At analysis time, the RMSE for MLoc is smaller than for SLoc for U,  $\theta$ , and particularly QVAPOR, while for QRAIN, SLoc performance is better. However, by the end of

the 1-h forecast, the MLoc-based forecast shows improvement over that of the SLoc. For all the fields but OVAPOR, it is worth noting that the difference between MLoc and SLoc is small at analysis time, but keeps increasing over the forecast. To further examine this, the RMSE ratio is shown in Fig. 8. Interestingly, the gains of MLoc over SLoc are generally largest at the end of the 1-h forecast experiment. This further illustrates the importance of propagating increments to nonprecipitating areas to achieve better forecasts with radar data assimilation and demonstrates that large-scale corrections add value to the forecast. Overall, for all the cases except case 1 (distributed showers) after the single cycle assimilation, MLoc improved over SLoc, with the highest gain in QVAPOR and the least gain in QRAIN for short forecast times; at longer forecast times, improvements in rain forecasts become the largest of all the fields considered.

The hydrometeors can be updated either using additive increments [Eq. (3)] or multiplicative increments [ $X_{HA} = X_{HB}(X_{SA}/X_{SB})$ ], the latter having the advantage of not creating negative precipitation and of boosting/lowering mixing ratios in cells. However, the hydrometeor fields were not updated in the first two steps because it was found that when additive [Eq. (3)] or multiplicative increments were added to the high-resolution backgrounds the performance of MLoc deteriorated. Our hypotheses for such a performance degradation are as follows:

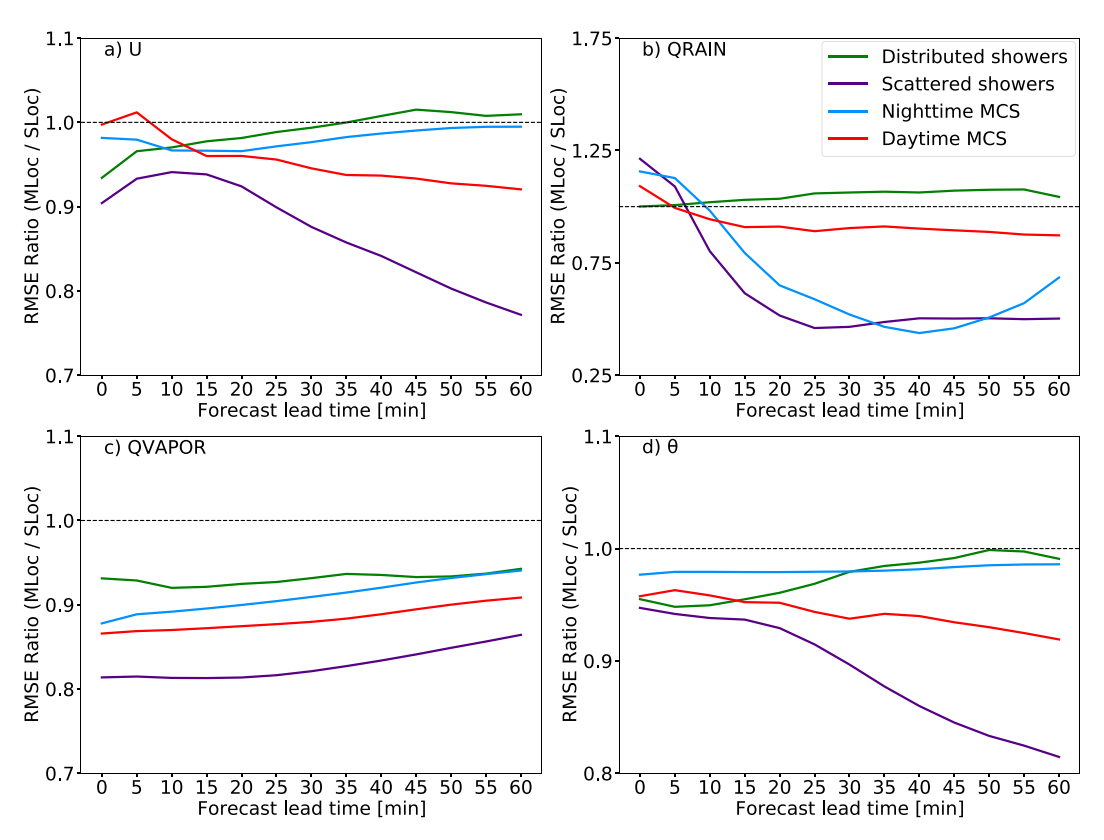


FIG. 8. RMSE ratio computed over each grid point for (a) U, (b) QRAIN, (c) QVAPOR, and (d)  $\theta$  for forecast lead time of 1 h after the first assimilation.

- 1) When additive innovation is used, weak positive and negative hydrometeor fields are added over large regions, resulting in either their removal for negative fields by the model or the DA system, leading to a bias in hydrometeor mixing ratio, or their evaporation and associated cooling for weak positive fields, creating a cool and moist bias.
- When multiplicative innovation is used, large positive precipitation innovations are concentrated in a few existing localized storms, creating unphysical background fields for the next assimilation step.

Thus, while optimum estimation theory would suggest innovating the hydrometeor fields, we could not find the best way to do it for the first two steps. We hence reluctantly chose not to innovate the hydrometeor fields at larger scales.

# b. Cycling assimilation experiment

Cycling experiments were then conducted. Since large-scale precipitation does not change as rapidly as precipitation at smaller scales and since the benefit of using the MLoc method comes from correcting errors at larger scales, the assimilation is performed every 30 min and the results of the experiments are shown after 2 h of cycling, that is, five assimilation cycles for both MLoc and SLoc experiments. Figure 9 shows the RMSE ratio for a 1-h forecast after the final assimilation for all the cases. For the Distributed shower case (case 1) MLoc performance is poorer than SLoc, whereas MLoc performs

better than SLoc for the other cases. For the Daytime MCS case (case 4), SLoc performs better than MLoc for  $\theta$  whereas MLoc performs better than SLoc for U, QVAPOR, and QRAIN. For the Distributed shower case (case 1) the performance of SLoc became gradually better than that of MLoc starting 30 min into the forecast; we believe that this can be attributed to the fact that, over many assimilation cycles, most of the domain is covered with precipitation and hence the SLoc is able to increment the grid points all over the model domain. Furthermore, the performance of SLoc was almost similar even in the single cycle experiment in most of the dynamical variables. A new experiment for case 1 was performed in which the Truth was drier and the precipitation did not cover the whole model domain. It was found that the MLoc performed better (results not shown) than SLoc in all the fields. This further illustrates the value of multiscale assimilation as the information from the storms is propagated to distant grid points.

# 4. Summary and conclusions

To improve forecasts at convective scales, lowering errors at medium to large scales is important. In contrast to synoptic-scale modeling, convective-scale modeling suffers from the combination of a rapid growth of forecasts errors and a lack of diversity of dense observations to constrain initial conditions. The convection and its associated precipitation, which are responsible for much of the initial growth of forecast

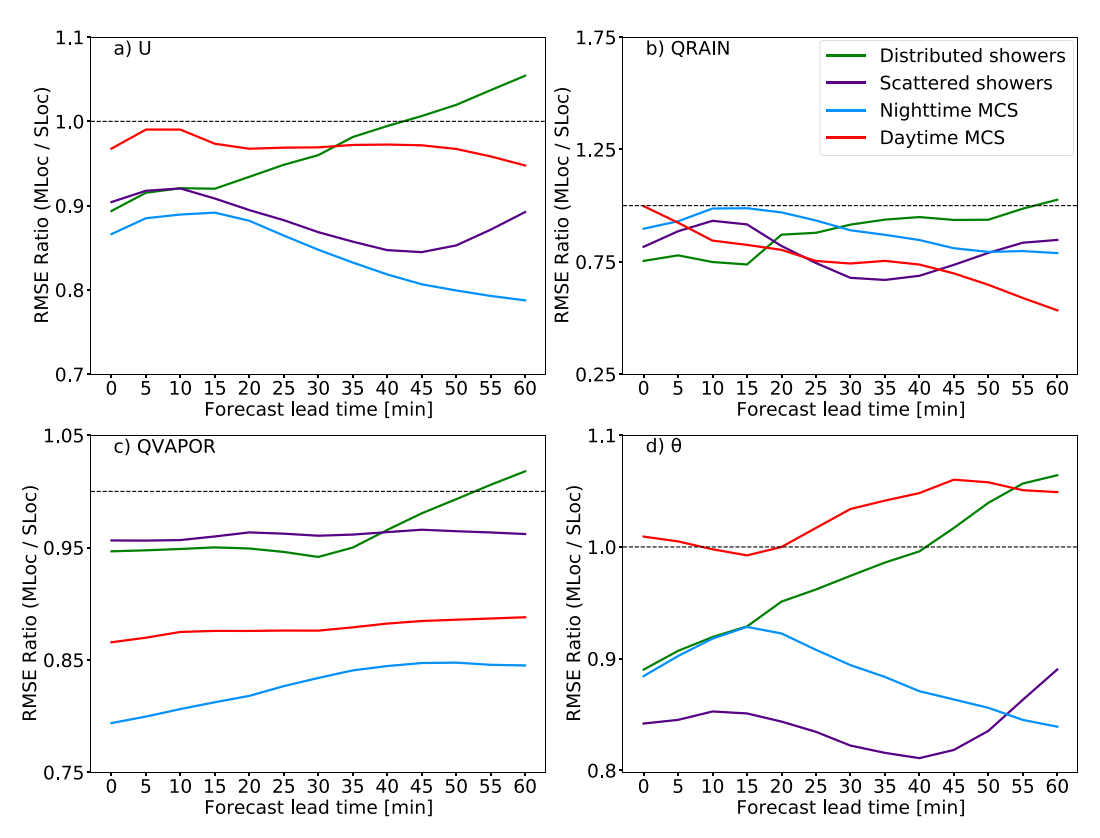


FIG. 9. As in Fig. 8, but for forecast lead time of 1 h after the final assimilation.

errors (Zhang et al. 2006), need to be adequately constrained with observations. High-resolution precipitation observations from radar contain information on smaller scales; this is important to correct small-scale errors. However, due to the clustered nature of precipitation, innovative observations are not available everywhere, if we ignore clear air echoes, and thus errors at large scales are difficult to correct. Furthermore, we believe the information from clear air echoes and that from large-scale precipitation are complementary: one provides direct constraints on winds; the other is better at indirectly constraining humidity fields (e.g., Fig. 9). Although with the use of larger localization radius in the EnKF, information could be spread from stormy regions to distant grid points, past experience has shown that the forecast skill is still poor, thus studies have recommended the use of shorter localization when assimilating radar observations. One reason for this is that the shorter correlation length scale for convection makes long-distance updates difficult to make because of sampling noise, which is why shorter localization radii are typically used; the correlation between fields are short-lived, resulting in continuous variability of relationships between them. Using information from the convectively active regions to correct fields in clear sky areas, where one can presume that errors are largely Gaussian and small, is likely to degrade the analysis quality. Alternatively, to spread information to distant grid points, inspiration can be drawn from techniques such as super-obbing. The benefits of averaging quantities are that they not only suppress small-scale variability but also increase the correlation length scales between fields

that can therefore be used to correct patterns over larger scales thanks to the use of larger localization radii.

To this end, in this paper, a new multiscale localization method named MLoc is developed wherein at each successive step different scales are corrected. This is achieved by smoothing the background members and observations (where the radius of smoothing depends on the scales of interest) for computing large- to medium-scale corrections. Finally for correcting all scales including the small scales, no smoothing is applied. The analyses obtained at each step are used as backgrounds for the next step. In doing so, by the end of the multiscale localization method, the final analyses obtained have multiple scales corrected. For this method, the EAKF is used to assimilate radar observations. Single cycle assimilation experiments and cycling assimilation experiments are conducted. In the cycling experiments, i.e., for the 2-h period, the SLoc and MLoc are cycled 5 times with an interval of 30 min between assimilation cycles. In general, for both the single cycle and cycling assimilation experiments, the multiscale approach produced superior forecasts, especially for longer lead times and when precipitation covers a small fraction of the domain. This multiscale approach is particularly adapted to radar (reflectivity) and satellite observations as both have high temporal and spatial resolutions that can be easily smoothed. The results from these experiments here corroborate the conclusion from previous multiscale localization studies that multiscale assimilation improves forecast skill. When assimilating only radar reflectivity using single-scale approaches, the precipitation field is improved

at analysis time, but the other fields are not sufficiently corrected when a short localization radius is used with a small ensemble size. MLoc adds value because new information concerning a precipitation pattern can change fields 100 km away while it otherwise would change state variables at most 10–20 km away. To increase the localization radius by a factor of 10 would require significantly larger ensemble.

While the large- and medium-scale correction with the MLoc method helps provide lasting gains in predictability, considerable errors in convective-scale forecasting remain. Small-scale patterns significantly contribute to the error growth due to their chaotic nature. When the NWP model is integrated forward in time, the small-scale errors dominate initially, contaminating the forecast. The lack of dense and diverse observations limits the error correction at these scales. While increasing the ensemble size is a solution, it is not easily feasible because of the cost associated with running high-resolution NWP model. To reduce error in convection with radar observations, more pragmatic measures may need to be explored when using the ensemble Kalman filter.

Acknowledgments. This project was undertaken with the financial support of the Government of Canada provided through the Department of the Environment through Grants and Contributions GCXE16S123. It was also enabled in part by support provided by Calcul Québec (https://www.calculquebec.ca) and Compute Canada (https://www.computecanada.ca).

Data availability statement. The software used in this research is publicly available. The analysis data used to generate the initial conditions of the model runs are from the HRRR data archive (https://doi.org/10.7278/S5JQ0Z5B; Blaylock et al. 2017). The data generated by the software are too large to be retained or publicly archived with available resources.

### REFERENCES

- Aksoy, A., D. C. Dowell, and C. Snyder, 2009: A multicase comparative assessment of the ensemble Kalman filter for assimilation of radar observations. Part I: Storm-scale analyses. *Mon. Wea. Rev.*, 137, 1805–1824, https://doi.org/ 10.1175/2008MWR2691.1.
- —, and —, 2010: A multicase comparative assessment of the ensemble Kalman filter for assimilation of radar observations. Part II: Short-range ensemble forecasts. *Mon. Wea. Rev.*, **138**, 1273–1292, https://doi.org/10.1175/2009MWR3086.1.
- Anderson, J. L., 2001: An ensemble adjustment Kalman filter for data assimilation. *Mon. Wea. Rev.*, **129**, 2884–2903, https://doi. org/10.1175/1520-0493(2001)129<2884:AEAKFF>2.0.CO;2.
- —, 2007: Exploring the need for localization in ensemble data assimilation using a hierarchical ensemble filter. *Physica D*, **230**, 99–111, https://doi.org/10.1016/j.physd.2006.02.011.
- —, T. Hoar, K. Raeder, H. Liu, N. Collins, R. Torn, and A. Avellano, 2009: The Data Assimilation Research Testbed: A community facility. *Bull. Amer. Meteor. Soc.*, 90, 1283–1296, https://doi.org/10.1175/2009BAMS2618.1.
- Blaylock, B. K., J. D. Horel, and S. T. Liston, 2017: Cloud archiving and data mining of High-Resolution Rapid Refresh

- forecast model output. *Comput. Geosci.*, **109**, 43–50, https://doi.org/10.1016/j.cageo.2017.08.005.
- Buehner, M., 2012: Evaluation of a spatial/spectral covariance localization approach for atmospheric data assimilation. *Mon. Wea. Rev.*, **140**, 617–636, https://doi.org/10.1175/MWR-D-10-05052.1
- —, and A. Shlyaeva, 2015: Scale-dependent background-error covariance localisation. *Tellus*, 67, 28027, https://doi.org/10. 3402/tellusa.v67.28027.
- Caron, J. F., and M. Buehner, 2018: Scale-dependent background error covariance localization: Evaluation in a global deterministic weather forecasting system. *Mon. Wea. Rev.*, 146, 1367–1381, https://doi.org/10.1175/MWR-D-17-0369.1.
- —, Y. Michel, T. Montmerle, and É. Arbogast, 2019: Improving background error covariances in a 3D ensemble-variational data assimilation system for regional NWP. *Mon. Wea. Rev.*, 147, 135–151, https://doi.org/10.1175/MWR-D-18-0248.1.
- Dawson, D. T., L. J. Wicker, E. R. Mansell, and R. L. Tanamachi, 2012: Impact of the environmental low-level wind profile on ensemble forecasts of the 4 May 2007 Greensburg, Kansas, tornadic storm and associated mesocyclones. *Mon. Wea. Rev.*, 140, 696–716, https://doi.org/10.1175/MWR-D-11-00008.1.
- Dowell, D. C., L. J. Wicker, and C. Snyder, 2011: Ensemble Kalman filter assimilation of radar observations of the 8 May 2003 Oklahoma City supercell: Influences of reflectivity observations on storm-scale analyses. *Mon. Wea. Rev.*, 139, 272–294, https://doi.org/10.1175/2010MWR3438.1.
- Emerick, A. A., and A. C. Reynolds, 2013: Ensemble smoother with multiple data assimilation. *Comput. Geosci.*, 55, 3–15, https://doi.org/10.1016/j.cageo.2012.03.011.
- Fabry, F., and V. Meunier, 2020: Why are radar data so difficult to assimilate skillfully? Mon. Wea. Rev., 148, 2819–2836, https://doi.org/10.1175/MWR-D-19-0374.1.
- Gaspari, G., and S. E. Cohn, 1999: Construction of correlation functions in two and three dimensions. *Quart. J. Roy. Meteor.* Soc., 125, 723–757, https://doi.org/10.1002/qj.49712555417.
- Hamill, T. M., J. S. Whitaker, and C. Snyder, 2001: Distance-dependent filtering of background error covariance estimates in an ensemble Kalman filter. *Mon. Wea. Rev.*, 129, 2776–2790, https://doi.org/10.1175/1520-0493(2001)129<2776: DDFOBE>2.0.CO;2.
- Houtekamer, P. L., and H. L. Mitchell, 2001: A sequential ensemble Kalman filter for atmospheric data assimilation. *Mon. Wea. Rev.*, **129**, 123–137, https://doi.org/10.1175/1520-0493 (2001)129<0123:ASEKFF>2.0.CO:2.
- —, and F. Zhang, 2016: Review of the ensemble Kalman filter for atmospheric data assimilation. *Mon. Wea. Rev.*, **144**, 4489–4532, https://doi.org/10.1175/MWR-D-15-0440.1.
- Iacono, M. J., J. S. Delamere, E. J. Mlawer, M. W. Shephard, S. A. Clough, and W. D. Collins, 2008: Radiative forcing by long-lived greenhouse gases: Calculations with the AER radiative transfer models. *J. Geophys. Res.*, 113, D13103, https:// doi.org/10.1029/2008JD009944.
- Janjić, Z. I., 1994: The step-mountain eta coordinate model: Further developments of the convection, viscous sublayer, and turbulence closure schemes. *Mon. Wea. Rev.*, 122, 927–945, https://doi.org/10.1175/1520-0493(1994)122<0927:TSMECM>2. 0.CO:2.
- Lorenc, A. C., 2003: The potential of the ensemble Kalman filter for NWP—A comparison with 4D-Var. *Quart. J. Roy. Meteor. Soc.*, **129**, 3183–3203, https://doi.org/10.1256/qj.02.132.
- Miyoshi, T., and K. Aranami, 2006: Applying a four-dimensional local ensemble transform Kalman filter (4D-LETKF) to the

- JMA Nonhydrostatic Model (NHM). *SOLA*, **2**, 128–131, https://doi.org/10.2151/sola.2006-033.
- —, and K. Kondo, 2013: A multi-scale localization approach to an ensemble Kalman filter. SOLA, 9, 170–173, https://doi.org/ 10.2151/sola.2013-038.
- Necker, T., M. Weissmann, Y. Ruckstuhl, J. Anderson, and T. Miyoshi, 2020: Sampling error correction evaluated using a convective-scale 1000-member ensemble. *Mon. Wea. Rev.*, 148, 1229–1249, https://doi.org/10.1175/MWR-D-19-0154.1.
- Periáñez, Á., H. Reich, and R. Potthast, 2014: Optimal localization for ensemble Kalman filter systems. *J. Meteor. Soc. Japan*, **92**, 585–597, https://doi.org/10.2151/jmsj.2014-605.
- Reisner, J., R. Rasmussen, and R. Bruintjes, 1998: Explicit fore-casting of supercooled liquid water in winter storms using the MM5 mesoscale model. *Quart. J. Roy. Meteor. Soc.*, 124, 1071–1107, https://doi.org/10.1002/qj.49712454804.
- Schwartz, C. S., G. S. Romine, M. L. Weisman, R. A. Sobash, K. R. Fossell, K. W. Manning, and S. B. Trier, 2015: A realtime convection-allowing ensemble prediction system initialized by mesoscale ensemble Kalman filter analyses. *Wea. Forecasting*, 30, 1158–1181, https://doi.org/10.1175/WAF-D-15-0013.1.
- Skamarock, W., and Coauthors, 2019: A description of the Advanced Research WRF Model version 4. NCAR Tech. Note NCAR/TN-556+STR, 145 pp., https://doi.org/10.5065/ 1dfh-6p97.
- Sobash, R. A., and D. J. Stensrud, 2013: The impact of covariance localization for radar data on EnKF analyses of a developing MCS: Observing system simulation experiments. *Mon. Wea. Rev.*, **141**, 3691–3709, https://doi.org/10.1175/MWR-D-12-00203.1.
- Tewari, M., and Coauthors, 2004: Implementation and verification of the unified Noah land surface model in the WRF model. 20th Conf. on Weather Analysis and Forecasting/16th Conf. on Numerical Weather Prediction, Seattle, WA, Amer. Meteor. Soc., 14.2a, https://ams.confex.com/ams/84Annual/techprogram/paper\_69061.htm.
- Thompson, G., P. R. Field, R. M. Rasmussen, and W. D. Hall, 2008: Explicit forecasts of winter precipitation using an

- improved bulk microphysics scheme. Part II: Implementation of a new snow parameterization. *Mon. Wea. Rev.*, **136**, 5095–5115, https://doi.org/10.1175/2008MWR2387.1.
- Wang, X., H. G. Chipilski, C. H. Bishop, E. Satterfield, N. Baker, and J. S. Whitaker, 2021: A multiscale local gain form ensemble transform Kalman filter (MLGETKF). *Mon. Wea. Rev.*, 149, 605–622, https://doi.org/10.1175/MWR-D-20-0290.1.
- Weng, Y., and F. Zhang, 2012: Assimilating airborne Doppler radar observations with an ensemble Kalman filter for convection-permitting hurricane initialization and prediction: Katrina (2005). Mon. Wea. Rev., 140, 841–859, https://doi.org/ 10.1175/2011MWR3602.1.
- Yang, S. C., S. H. Chen, K. Kondo, T. Miyoshi, Y. C. Liou, Y. L. Teng, and H. L. Chang, 2017: Multilocalization data assimilation for predicting heavy precipitation associated with a multiscale weather system. J. Adv. Model. Earth Syst., 9, 1684–1702, https://doi.org/10.1002/2017MS001009.
- Ying, Y., 2019: A multiscale alignment method for ensemble filtering with displacement errors. *Mon. Wea. Rev.*, 147, 4553– 4565, https://doi.org/10.1175/MWR-D-19-0170.1.
- —, 2020: Assimilating observations with spatially correlated errors using a serial ensemble filter with a multiscale approach. *Mon. Wea. Rev.*, **148**, 3397–3412, https://doi.org/10. 1175/MWR-D-19-0387.1.
- —, F. Zhang, and J. L. Anderson, 2018: On the selection of localization radius in ensemble filtering for multiscale quasigeostrophic dynamics. *Mon. Wea. Rev.*, **146**, 543–560, https:// doi.org/10.1175/MWR-D-17-0336.1.
- Zhang, F., A. M. Odins, and J. W. Nielsen-Gammon, 2006: Meso-scale predictability of an extreme warm-season precipitation event. Wea. Forecasting, 21, 149–166, https://doi.org/10.1175/WAF909.1.
- —, Y. Weng, J. A. Sippel, Z. Meng, and C. H. Bishop, 2009: Cloud-resolving hurricane initialization and prediction through assimilation of Doppler radar observations with an ensemble Kalman filter. *Mon. Wea. Rev.*, 137, 2105–2125, https://doi.org/10.1175/2009MWR2645.1.